Catalysis Science & Technology

Accepted Manuscript

ROYAL SOCIETY OF CHEMISTRY

www.rsc.org/catalysis

Plasmon-Enhanced Reverse Water Gas Shift Reaction over Oxide Supported Au Catalysts

Aniruddha A. Upadhye[a], Insoo Ro[a], Xu Zeng[a], Hyung Ju Kim[a], Isabel Tejedor[b], Marc A. Anderson[b], James A. Dumesic[a], George W. Huber[a,]*

Abstract

We show that localized surface plasmon resonance (LSPR) can enhance the catalytic activities of different oxide-supported Au catalysts for the reverse water gas shift (RWGS) reaction. Oxide-supported Au catalysts showed 30 to 1300% higher activity for RWGS under visible light compared to dark conditions. Au/TiO_2 catalyst prepared by deposition-precipitation (DP) method with 3.5 nm average Au particle size showed the highest activity for the RWGS reaction. Visible light is converted into chemical energy for this reaction with up to a 5 % overall efficiency. A shift in the apparent activation energy (from 47 kJ/mol in dark to 35 kJ/mol in light) and apparent reaction order with respect to CO_2 (from 0.5 in dark to 1.0 in light) occurs due to the LSPR. Our kinetic results indicate that the LSPR increases the rate of either the hydroxyl hydrogenation or carboxyl decomposition more than any other steps in the reaction network.

1.0 Introduction

Environmental concerns over anthropogenic CO_2 emissions combined with increased petroleum costs are causing our society to develop new sustainable methods for production of renewable transportation fuels and commodity chemicals. Technology breakthroughs in photovoltaics are making solar-driven electricity production more efficient[1-3]. This renewable electricity could be used to produce hydrogen via water electrolysis[4]. There are several other approaches being developed to produce hydrogen directly from solar photoelectrochemical water splitting[1, 2, 4-8]. However, hydrogen cannot power heavy machinery including jet and diesel engines. Furthermore, using hydrogen in an internal combustion engine would require a major change in the existing infrastructure. Liquid carbon-based fuels are the preferred fuel option for the transportation sector because they: (1) are easy to store, (2) have an established distribution infrastructure, and (3) have higher energy density. Ideally, renewable hydrogen can be reacted with carbon dioxide to produce liquid fuels in an economically viable process. Thus, the area of CO_2 reduction to fuels and chemicals has recently received significant attention[9-12]. The first step of reduction of CO_2 using H_2 is the reverse water gas shift (RWGS) reaction as shown in Equation 1. This reaction is endothermic with a standard heat of reaction as 41.27 kJ/mol.

$$CO_2 + H_2 \leftrightarrow CO + H_2O \qquad \Delta H^0 = 41.27\ \text{kJ/mol} \qquad (1)$$

The carbon monoxide produced in the RWGS reaction can then be upgraded to “drop-in” transportation fuels and chemicals through mature technologies such as methanol synthesis and Fischer-Tropsch synthesis[13]. Both of these downstream processing options are exothermic. Thus, RWGS reaction is the only energy intensive reaction involved in catalytic reduction of CO_2 to useful fuels and chemicals. Hence, it would be highly desirable to develop photocatalytic processes which would provide energy for the RWGS reaction from solar energy.

---

[a]Department of Chemical and Biological Engineering, University of Wisconsin-Madison, 53706
[b]Department of Civil and Environmental Engineering, University of Wisconsin-Madison, 53706
*Corresponding Author (huber@engr.wisc.edu)

Solar energy is the ultimate source of renewable energy. The amount of solar energy intercepted by the earth in one hour (4.3×10^{20} J) is sufficient to satisfy the annual global energy consumption (4.1×10^{20} J)[2, 14]. For the past few decades researchers have been trying to harness solar energy to drive chemical reactions for fuel production using inorganic materials. Traditionally, photocatalytic reactions have been carried out over semiconductor based materials[4, 8]. Most of these materials are photocatalytically active in the ultraviolet (UV) region. Only 4% of solar spectrum contains UV radiation, while 46% of the solar energy is contained in the visible part of the solar spectrum. Numerous approaches including doping[15], quantum confinement[16], dye-sensitization[17, 18] have been proposed to move semiconductor based photocatalysis in visible range and this remains one of the most researched areas in solar energy conversion.

Recent studies have shown that the phenomenon of localized surface plasmon resonance (LSPR) can be applied to catalytic reactions to enhance the activity of LSPR exhibiting materials under visible light illumination[19-25]. The phenomenon of LSPR occurs when the size of metal particle is in the range of the penetration depth of the light for that metal[26]. For metals such as gold, copper, silver etc. the light penetration depth is around 25 nm[26]. As a result of LSPR, three main effects have been reported to arise in a plasmonic material[23, 27]: (1) localized heating, (2) enhanced electromagnetic fields, and (3) electron-hole pair generation. All of these three effects have been proposed to enhance the activity of catalytic materials[23, 27]. One of the advantages of plasmonic catalysts is that the LSPR frequency is a strong function of type of metal, and structure (i.e. size and shape) of the metal nanoparticle[28-30]. This behavior allows the engineering of catalytic materials to increase the light absorption in the visible region. Au, Ag, and Cu are considered the most promising plasmonic materials because of their (i) optical properties (i.e. low loss factor and LSPR frequency in the visible range) and (ii) catalytic properties for certain reactions[19].

The primary objective of this paper is to elucidate how LSPR can be used to change the kinetics of the endothermic RWGS reaction for CO_2 reduction. In addition, we will demonstrate how visible light can be used to drive this reaction. It has previously been reported that visible light can enhance the activity for WGS on Au/TiO_2 catalysts[21] and CO2 reduction on Au/ZnO catalyst[31]. Thus, we anticipate that the Au/TiO_2 catalyst would be active for RWGS reaction as well. However, it is unknown how the plasmons change the intrinsic kinetics of these surface reactions[30].

2.0 Experimental

2.1 Reactor and analytical setup

Figure 1 shows the experimental setup used to measure the activity of different catalysts for RWGS reaction. The flow rate for the reactant gases CO_2 and H_2, and inert gas He were controlled using Cole-Parmer mass flow controllers (FF-32907-59). Research grade CO_2 (CDR200), Ultra high purity (UHP) H_2 (UHP HY300) and He (UHP HE300) gas cylinders from Airgas were used. The reactor was purchased from Harrick scientific (HVC-MRA-5) and operated in the temperature range of room temperature to 400 °C and pressures up to 150 psi. 3-30 mg of catalyst was loaded in the heater cup of the Harrick reactor as shown in Figure 1. The bottom part of the cup was loaded with the catalyst support which showed minimal catalyst activity as described below. Only the top 1-2 mm of the cup were loaded with the catalyst to ensure illumination of catalyst bed. The reactor had SiO_2 windows which allowed catalyst illumination with visible light. The temperature of the catalyst bed was controlled by a PID temperature controller. The heating block was located at the bottom of the catalyst bed, while the window of the reactor was exposed to room temperature as seen in Figure 1. To measure the temperature gradient, the heater cup was filled with sand (about 5 mm depth). The window of the reactor was removed and temperature of the sand was measured ex-situ with another thermocouple. This temperature gradient was estimated as the difference between sand temperature and the set point temperature. The gradient was less than 10% of the set point temperature as measured in °Celsius (e.g. the sand bed temperature was 366 °C at set point temperature of 400 °C). The difference in apparent activation energy values calculated with the temperature gradient and without the temperature gradient was only 6%. The temperature had a small effect on the apparent reaction order, i.e. we obtained apparent rate order with respect to CO_2 as 0.5 at set point temperature of 200 °C and 0.6 at 260 °C. These results show that the temperature gradient did not affect our measurement of apparent activation energy or apparent reaction orders. The reactor pressure was maintained using a back pressure regulator. The product gas flow rate was measured by a bubble flow meter.

The composition of the product gases was analyzed by an online Shimadzu-gas chromatograph with barrier discharge ionization detector (GC-BID) system with auto-sampling 6-port valve. The BID uses a helium plasma to detect permanent gases such as CO_2, CO, H_2 with high sensitivity. The products were separated using four different columns in the GC. First, all the gases were passed through Haysep T and Q Bond column to separate CO_2 and organics from permanent gases such as CO, H_2, CH_4, N_2 and O_2. The permanent gases which elute early were loaded on the molecular sieve column. The remaining gases flowing through Q Bond column were sent to the BID through the Shim Q column to detect CO_2 and other organics. After achieving elution of all the organics from the Q Bond and Shim Q columns, permanent gases from molecular sieve column were sent to the BID to detect gases such as H_2, O_2, N_2, CO, and methane. The GC-BID system was calibrated using Scotty specialty gases (P/N 34507 and 34512).

The catalyst bed was illuminated using a Dolan-Jenner broadband visible light source (MI-150) with fiber optic cable as shown in Figure 1. The intensity and spectral distribution of the light were measured using NIST-traceable, ISO-17025 calibrated spectroradiometer (ILT950) from International Light Technologies. For this measurement, the light passed through the SiO_2 window to account for losses in transmission through the window. Using this setup the light intensity reaching the catalyst bed was measured as 5216 W/m^2 (refer to Figure S1 for spectral distribution of the light). For dark reaction, the window was covered with an opaque metal disc as seen in Figure 1.

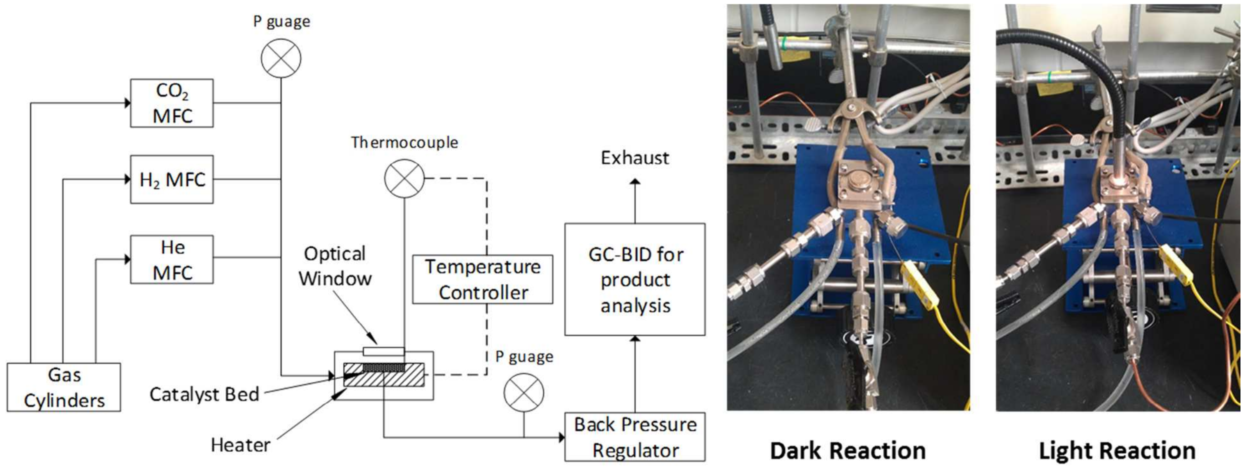

Figure 1. Experimental setup for test of activity of different catalyst for RWGS reaction under light and dark conditions

2.2 Catalyst synthesis

Catalyst investigated in this study were prepared by deposition-precipitation (DP)[32-34] and impregnation (I) methods[21, 35]. The Au/TiO_2 (DP), Au/CeO_2 (DP), and Au/Al_2O_3 (DP) catalysts were prepared by deposition-precipitation (DP) method[32-34]. Degussa P25 TiO_2 (Aldrich, >99.5%), CeO_2 (Aldrich), and Al_2O_3 (Strem Chemicals) were used as supports. $HAuCl_4 \cdot 3H_2O$ (Aldrich, >99.9% trace metal basis) was used as the precursor for Au catalysts, while $CuSO_4 \cdot 5H_2O$ (Aldrich, 99-100.5%) was used as a precursor for the Cu/TiO_2 catalyst. For preparation of supported Au catalysts by DP method, supports (i.e. TiO_2, CeO_2 and Al_2O_3) were dried in the air at 110 °C overnight. One hundred ml of aqueous $HAuCl_4$ solution (4.2×10^{-3} M) was heated to 80 °C and the pH was adjusted to 8 by drop-wise addition of NaOH (1 M). Then, 1 g of support was dispersed in the solution, and the pH was readjusted to 8 with NaOH. The suspension was maintained at 80 °C with continuous stirring. After 2 h the suspension was centrifuged. The solids were then washed, dried, and calcined at 300 °C under the flow of air (30 cm^3(STP)/min) with a heating rate of 2 °C/min and maintained for 4 h. The Cu/TiO_2 (I) catalyst was prepared by impregnating 1 g of TiO_2 with a solution of 53 mg of $CuSO_4 \cdot 5H_2O$ in 10 ml of DI water[21, 35]. The slurry was stirred for 4 h at room temperature, then all liquid was evaporated and the solid was dried at 110 °C overnight. The catalyst was calcined at 300 °C under flowing air (30 ml/min) with a heating rate of 2 °C/min and maintained for 4 h. Prior to the reactions, the catalysts were reduced in-situ under flowing H_2 (10 cm^3(STP)/min) with a heating rate of 1 °C/min and maintained for 2 h at 300 °C.

2.3 Catalyst characterization

The metal loadings of the catalysts were measured using Inductively Coupled Plasma (ICP) analysis. For ICP analysis, 8-10 mg of the catalyst was dissolved in an acid solution of HF, HCl, and HNO_3 in a Teflon beaker at 110 °C until the particles dissolved. The Au ions were detected using Perkin Elmer Plasma 400 ICP emission spectrometer. Gold (2.5-25 ppm) standards were prepared from a purchased Au 1000 ppm standard (38168, Fluka). The amount of Cu on Cu/TiO_2 catalyst was estimated from the $CuSO_4$ amount used during impregnation as all of the Cu is deposited on the support in this procedure. The synthesized catalysts were characterized using transmission electron microscopy (TEM) to obtain the particle size distribution of the Au. A Tecnai T12 TEM at 120 kV was used for TEM analysis. The light absorption of the catalyst was characterized using diffuse reflectance ultra-violet visible spectroscopy. Thermo Scientific Evolution 300 UV-Vis spectrometer was used with Praying Mantis diffuse reflectance accessory to collect UV-Visible absorption data.

3.0 Results

3.1 Catalyst Characterization

Table 1 shows the RWGS activity of different Au and Cu catalysts supported on different oxides such as TiO_2, CeO_2, and Al_2O_3 with and without light. The metal loading of the catalysts was estimated using ICP analysis post-catalyst synthesis. Using TEM analysis, the Au particle size for the catalysts was estimated to be between 3 to 11 nm as shown in Figure 2. The gold metal nanoparticles in these size ranges have been shown to exhibit LSPR[27]. For example, Garcia and co-workers have observed LSPR with 3-5 nm size Au particles for water gas shift reaction[21]. The LSPR was further characterized by UV-Visible extinction spectra as seen in Figure 3. The absorption peak around 520-580 nm is clearly seen in all the Au catalysts corresponding to LSPR of Au nanoparticles. Difference in peak area and height can be attributed to the different gold loading amounts. For Cu/TiO_2 catalyst, a sharp LSPR peak like Au-based catalyst is not seen in Figure 3 (a). This behavior is consistent with the literature that shows Cu has a lower light absorption compared to Au due to lower absorption coefficient of Cu[19, 36, 37]. As seen from the Figure 3, all the metal supported catalysts show increased visible light absorption compared to their supports.

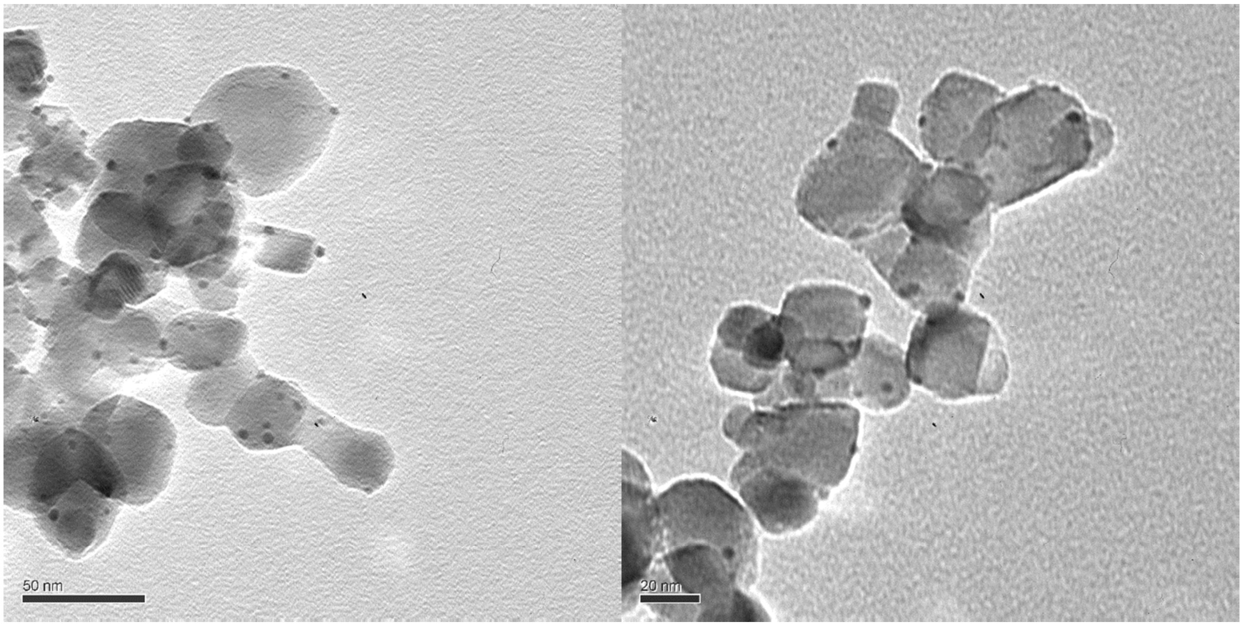

Figure 2. Transmission Electron Microscopic (TEM) pictures of Au/TiO_2 prepared by deposition precipitation (DP) method

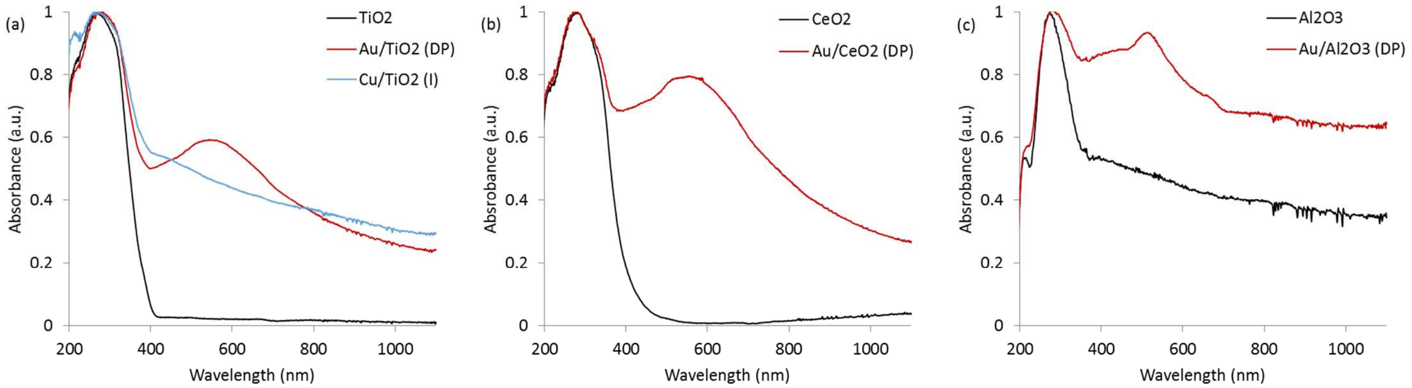

Figure 3. Diffuse reflectance UV-visible absorption spectra for **(a)** TiO_2 supported catalysts: (i) TiO_2 support, (ii) Au/TiO_2 (DP), (iii) Cu/TiO_2 (I); **(b)** CeO_2 supported catalysts: (i) CeO_2 support and (iii) Au/CeO_2 (DP); and **(c)** Al_2O_3 supported catalysts: (i) Al_2O_3 support, (ii) Au/ Al_2O_3 (DP)

3.2 Activity of different catalysts for plasmon-enhanced RWGS reaction

The activity of the catalysts was measured at 400 °C and 2:1 H_2 to CO_2 molar ratio. The Au/TiO_2 (DP) catalyst had the highest activity for RWGS reaction with and without light as seen in Table 1. The activity of Au catalysts for water gas shift reaction has been reviewed extensively in the literature[38-40]. It is known that metallic Au by itself is a poor catalyst for WGS reaction but when supported on oxides supports like TiO_2 and CeO_2, the activity of Au catalysts increases[41-44]. Similar results were obtained in this study in dark conditions, in which Au/TiO_2 and Au/CeO_2 showed the highest activity, while Au/Al_2O_3 showed low activity. The TiO_2, CeO_2, and Al_2O_3 supports, by themselves, exhibited low activity for RWGS reaction. All of the metal supported catalysts showed higher activity under light compared to dark. The plasmonic enhancement of the CO_2 conversion rate was described by two parameters: (i) the difference between reaction rates under light and dark (rate difference), and (ii) the ratio between the reaction rate under light to dark (rate enhancement). The Au/CeO_2 had the maximum rate difference between the light and dark reaction rates of 761 μmol/gm-cat/min at 400 °C followed by Au/TiO_2 (DP). Au/Al_2O_3 (DP) and Cu/TiO_2 (I) catalysts showed low activity in both light and dark conditions that were comparable to the supports themselves. The Au/CeO_2 catalyst showed the maximum rate enhancement of 2.2, followed by Au/Al_2O_3 (DP), Au/TiO_2 (DP) and Cu/TiO_2 (I) catalysts. All of these catalysts showed at least 30% higher rates under light compared to dark conditions. Because of the inherent high activity of Au/TiO_2 (DP) catalyst under light and dark, the performance of Au/TiO_2 catalyst was investigated further.

Table 1. Activity of different catalysts for plasmon-enhanced reverse water gas shift reaction. Experimental conditions: P= 110 psi, T= 400 °C, PP_{CO_2}=36.7 psi, PP_{H_2}= 73.3 psi, Total flow rate= 15 cm^3(STP)/min

Sr. No.	Catalyst	Metal loading[a] (wt%)	Metal particle size[b] (nm)	Catalyst amount (mg)	CO_2 conversion rate (µmol/gm-cat/min)			Enhancement (Light/Dark)
					Dark	Light	(Light-Dark)	
1	Au-TiO_2 (DP)	1.4	3.5±1.0	7.4	2033	2663	630	1.3
2	Au-CeO_2 (DP)	3.3	5.0±1.2	12.8	656	1417	761	2.2
3	Au-Al_2O_3 (DP)	0.7	10.9±4.7	16.6	77	118	42	1.5
4	Cu-TiO_2 (I)	1.3	15 to 30[c]	8.6	20	25	6	1.3
5	TiO_2	0	NA	12.2	21	19	-2	0.9
6	CeO_2	0	NA	23.9	21	22	1	1.0
7	Al_2O_3	0	NA	30.0	67	74	6	1.1

[a]Au loading was measure by ICP analysis, Cu loading was calculated from amount of Cu precursor used during synthesis; [b]Particle size of Au was estimated using TEM analysis; [c]Particle size Cu estimated based on literature Ref[21]; NA: Not Applicable

3.3 Reaction kinetics studies on Au/TiO_2 catalysts

The effect of heat and mass transport were estimated for our system using the dimensionless criteria shown in Table S1[45-47]. Reaction data (i.e. reaction rate, activation energy, heat of reaction, reaction order) under dark conditions at 200 °C, 110 psi pressure and a 2:1 molar H_2 to CO_2 ratio were used for these calculations. Heat and mass transfer coefficients and material properties were estimated using correlations available in the literature[47-49]. A catalyst particle size of 150 µm was used for these calculations. This particle size was estimated from sieving analysis. All of the computed values for estimating intraparticle and interphase heat and mass transfer limitations are smaller than the controlling regime criteria. For example, the calculated intraparticle mass transfer number or Weisz-Prater number for the system was 5.9×10^{-8} suggesting the absence of intraparticle pore diffusion limitations[46, 50]. The pore diffusion limitations are dominant for Weisz-Prater numbers above 0.3[46, 50]. Thus, these reactions were carried out in the absence of any mass or heat transport limitations.

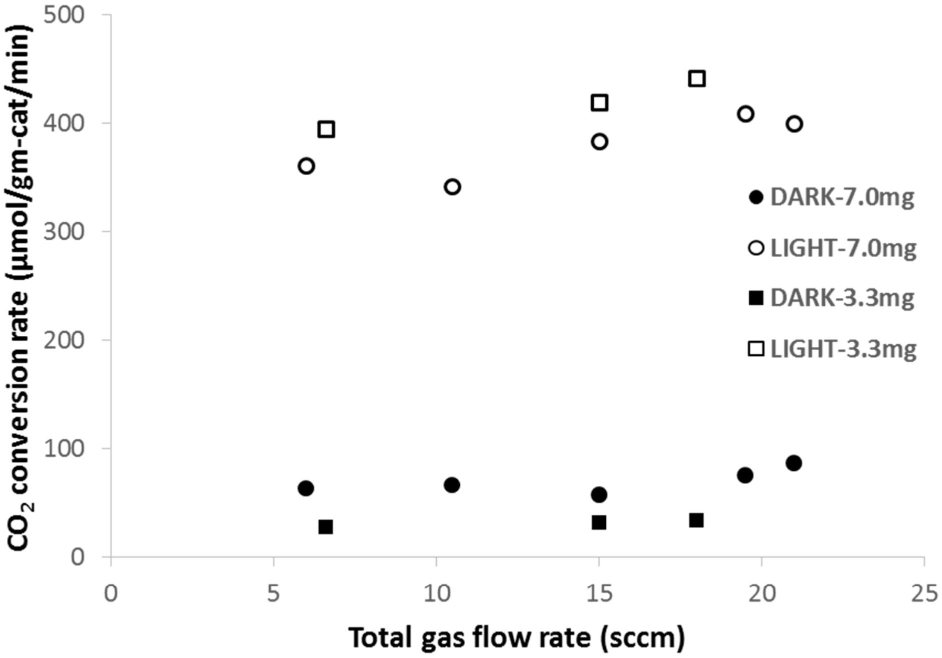

Figure 4: Dependence of CO_2 conversion rate on total gas flow rate in plasmon enhanced RWGS reaction over Au/TiO_2 catalyst under light and dark conditions. Experimental conditions: P= 110 psia, T=200 °C, PP_{CO_2}=36.7 psi, PP_{H_2}= 73.3 psi, catalyst amounts= 7 mg and 3.3 mg.

The reactor was operated in differential mode at low conversions, typically less than 5% and also less than 30% of the thermodynamic limit. For example, at 200^{o}C the conversion was about 1% which is below the thermodynamic limit of 9%. At 300^{o}C the conversion was about 4% which is below the thermodynamic limit of 21%. The CO_2 conversion rate was independent with respect to total gas flow rate under both light and dark as shown in Figure 4. These experiments are consistent with our calculations that suggest that external mass and heat transfer were negligible in these studies. To investigate light transfer limitations, the depth of the catalyst bed was varied by loading 3.3 and 7 mg of the catalyst. As seen by Figure 4, the reaction rates under light for 3.3 and 7 mg catalyst loading were similar. This result indicates that even at higher 7 mg catalyst loading, most of the catalyst bed was illuminated by the light. Thus, we ensured that the reactor was operated in absence of mass, heat and light transport limitations to obtain intrinsic kinetic data for the reaction.

3.3.1 Effect of temperature on the activity of Au/TiO_2 catalyst for RWGS

The temperature of the reaction was varied between 100 to 400 °C at constant pressure as shown in Figure 5 (a). We observed that the reaction rate was higher with light compared to dark at all temperatures tested. Figure 5 (b) shows that the rate enhancement decreased as the temperature increased from 100 to 400 °C. These results indicate that the plasmonic effect becomes less dominant with increasing temperature. The rate enhancement below 175 °C cannot be calculated because the catalytic activity under dark condition at this temperature is too low to be detected with GC. Figure 5 (c) shows that the difference between light and dark reactions increases with temperature in the temperature range of 100 to 325 °C and decreases beyond 325 °C.

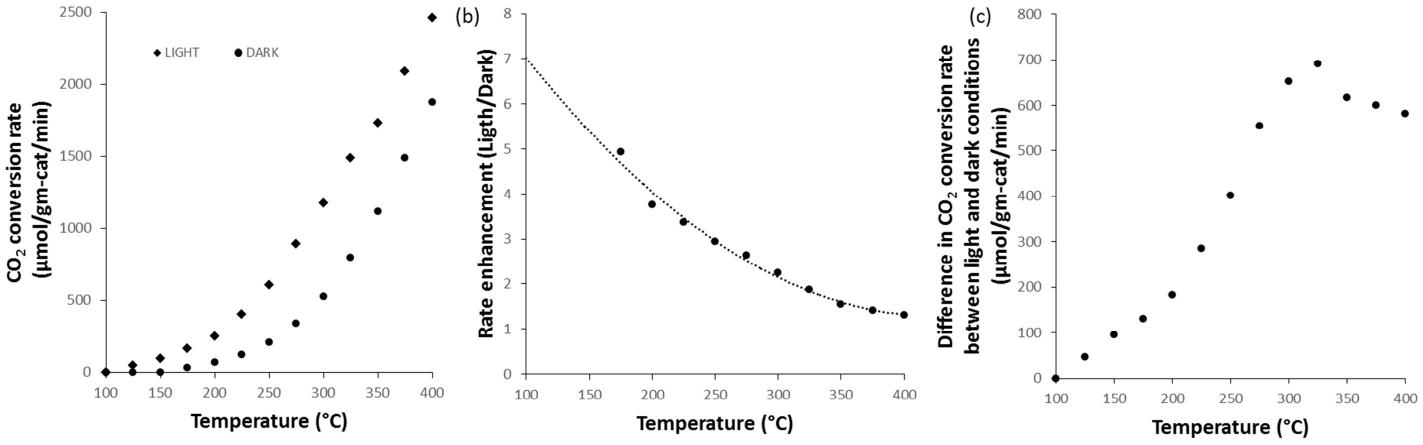

Figure 5. Temperature dependence of CO_2 conversion rate plasmon-enhanced reverse water gas shift reaction over Au/TiO_2 (DP) catalyst: **(a)** CO_2 conversion rate vs temperature under light and dark conditions; **(b)** Rate enhancement i.e. ratio of CO_2 conversion rate under light to CO_2 conversion rate under dark condition vs temperature; **(c)** Difference in CO_2 conversion rate between light and dark conditions vs temperature. Experimental conditions: P= 110 psi, PP_{CO_2}=36.7 psi, PP_{H_2}= 73.3 psi, Total flow rate= 15 cm^3(STP)/min, catalyst amount= 7.4 mg

The Au/TiO_2 catalyst was characterized before and after reaction using UV-Vis spectroscopy and TEM imaging. Figure 6 (a) shows that the Au LSPR peak slightly red-shifted after the reaction. Figure 6 (b) shows that the Au particle size distribution increases slightly after reaction. These results indicate that the catalyst did not undergo major structural change during the reaction.

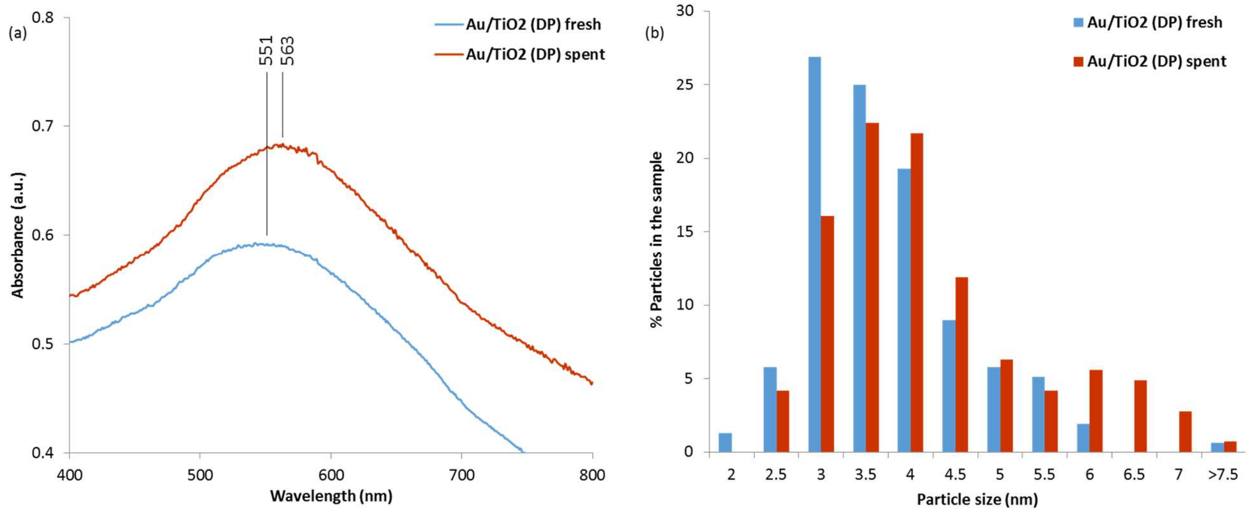

Figure 6. (a) Diffuse reflectance UV-visible absorption spectra for Au/TiO_2 (DP) fresh and Au/TiO_2 (DP) spent catalyst; **(b)** particle size distribution obtained from TEM image analysis of Au/TiO_2 (DP) fresh and spent catalysts

The reaction rate versus temperature data were plotted in an Arrhenius plot as seen in Figure 7. The apparent activation energy for the RWGS reaction over Au/TiO_2 catalyst decreased from 47 kJ/mol under dark conditions to 35 kJ/mol with visible light. This change in apparent activation energy suggests that the LSPR is changing the energetics of the reaction. One theory that has been proposed to explain these effects is that plasmons induce localized heating[31, 51-53]. Govorov and Richardson estimated temperature rises of less than 1 °C for colloidal gold nanoparticle solution under similar light intensities[54]. In our system, the heat dissipation from the plasmonic Au nanoparticle would be even faster due to faster conductive heat transfer in TiO_2 support compared to convective heat transfer in colloidal Au solutions. Thus, the local temperature rise in our system should be even smaller than 1 °C. To observe such a large increase in rate due to localized heating effect, a local temperature rise of greater than 50 °C would be needed (see Figure 5 (a)). Hence, localized heating effects cannot explain the plasmonic enhancement of the reaction rate. In addition, if only localized heating were responsible for this enhancement, then the apparent activation energy for the reaction would remain the same under light and dark conditions with such small temperature rises.

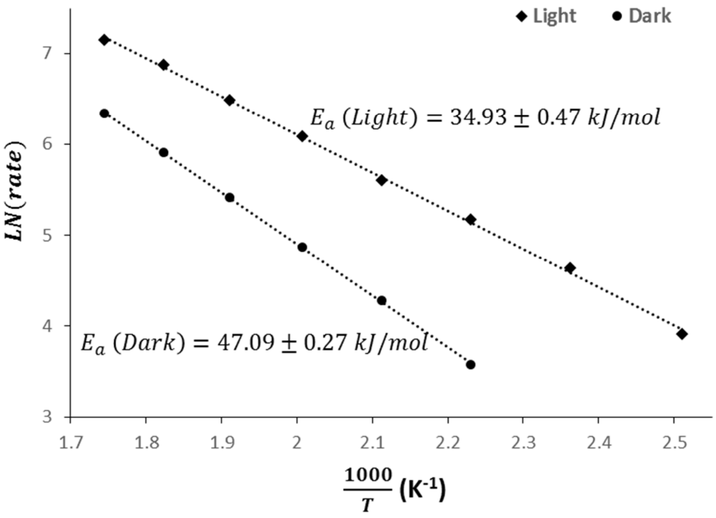

Figure 7. Arrhenius plot for CO_2 conversion rate under light and dark conditions for plasmon-enhanced reverse water gas shift reaction over Au/TiO_2 (DP) catalyst. Experimental conditions: P= 110 psi, PP_{CO_2}=36.7 psi, PP_{H_2}= 73.3 psi, Total flow rate= 15 cm^3(STP)/min, catalyst amount= 7.9 mg

3.3.2 Effect of CO_2 and H_2 partial pressure on activity of Au/TiO_2 catalyst for RWGS reaction

The dependence of the reaction rate on CO_2 and H_2 partial pressures was investigated to gain more insights into how plasmons influence the reaction mechanism. Figure 8 (a) shows the dependence of the reaction rate on the CO_2 partial pressure under light and dark conditions at constant H_2 partial pressure. The reaction order with respect to CO_2 changes from 0.5 under dark conditions to 1.0 under light. These results can be interpreted using Hougen-Watson type models for heterogeneous catalytic reaction based on Langmuir adsorption[47, 55]. According to this model, a reaction order of less than 1 indicates the presence of adsorbed surface species inhibiting the rate of the reaction[47]. Thus, under dark conditions, the reaction rate could be inhibited by adsorbed CO_2 species or intermediates produced from the CO_2 on the catalytic surface. The increase in order with respect to CO_2 to 1 under light suggests that the inhibition due to surface coverage of adsorbed species is reduced by the LSPR. Under dark conditions, temperature had little effect on the apparent reaction order with respect to CO_2. Similar apparent reaction orders with respect to CO_2 were obtained at 260 °C (n=0.6) and 200 °C (n=0.5) under dark conditions.

Figure 8 (b) shows the dependence of reaction rate on H_2 partial pressure under light and dark conditions at constant CO_2 partial pressure. As seen from Figure 8 (b), the reaction rate is a weak function of the H_2 partial pressure. The order of the reaction with respect to H_2 only slightly changes from 0.07 in dark conditions to 0.17 under light. In Hougen-Watson models, such behavior is observed under high surface coverage of adsorbed species when the reacting molecule is readily adsorbed on the catalyst surface[47]. This observation is consistent with FTIR studies by Boccuzzi and co-workers, who showed that H_2 dissociatively adsorbed strongly on edge and corner Au sites[56]. In the study, they found that formation of Au-H and Au-OH species due to adsorption of hydrogen on metallic Au sites and sites in contact with oxide support[56]. Spillover of H atoms was also observed in their study with monotonous increase in H adsorption with contact time and pressure[56].

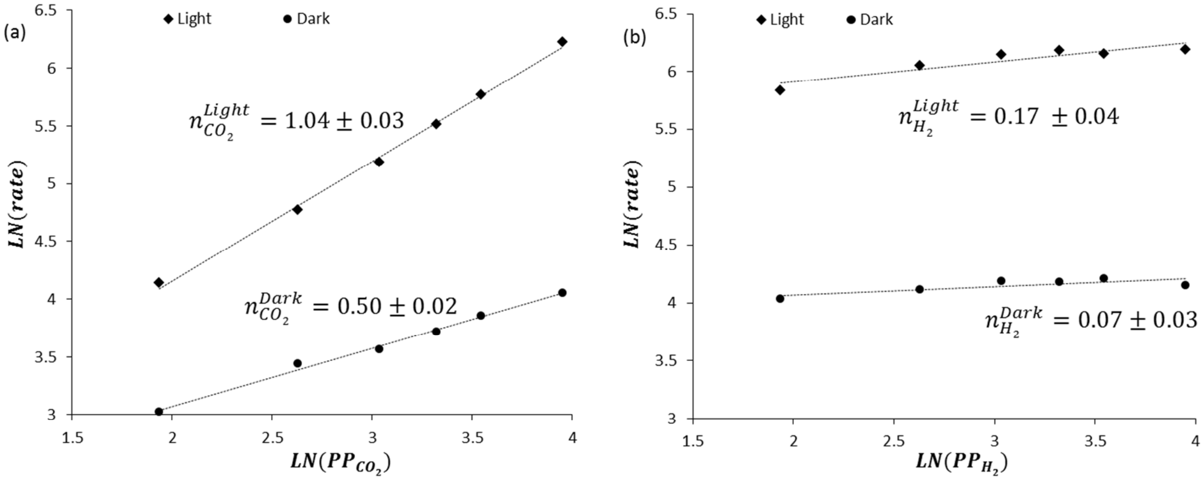

Figure 8. Dependence of CO_2 conversion rate in plasmon-enhanced reverse water gas shift reaction on **(a)** CO_2 partial pressure and **(b)** H_2 partial pressure under light and dark conditions over Au/TiO_2 (DP) catalyst. Experimental conditions: P= 104 psi, Total flow rate= 15 cm^3(STP)/min, T=200 °C, catalyst amount= 7.9 mg, partial pressure of the other reactant kept constant at 52 psi using He as an inert gas.

3.3 Light to chemical energy efficiency

We calculate the light to chemical energy efficiency by assuming that the difference in reaction rates under light and dark conditions results from the light input given by Equation 2. The difference in CO_2 conversion rate (Light-Dark) is the difference between reaction rates under light and dark conditions. $\Delta H_{reaction}$ is the heat of the reaction ($\Delta H_{reaction}$ = 41.27 kJ/mol), Intensity is the intensity of light input to the reactor (5216 W/m^2) and catalyst surface area is the cross sectional area of the catalyst bed exposed to incoming light radiation. The heat of reaction changes slightly from 41.27 kJ/mol at room temperature to 38.35 kJ/mol at 400 °C. This weak dependence of heat of the reaction on temperature was neglected in these calculations. We further validated this assumption by measuring the energy input to the heater from the temperature controller. The energy input from the heater was, in fact, lower under light compared to dark conditions. This result indicated that the light input did not just catalyze the reaction but also provided the energy for the endothermic reaction.

$$\textbf{Light efficiency}\ (\%) = \frac{Difference\ in\ CO_2\ conversion\ rate\ (Light - Dark) \times \Delta H_{reaction}}{Intensity \times Catalyst\ surface\ area} \times 100\% \qquad (2)$$

In Figure 9 (a) we estimate the corresponding light to chemical efficiency. The light efficiency increases with temperature up to 325 °C and then decreases beyond 325 °C. The maximum efficiency for the process is obtained at 325 °C as 4.5%. This efficiency is higher than values reported in the literature for other photocatalytic CO_2 reduction processes[57]. Most photocatalytic CO_2 reduction approaches focus on aqueous phase conversion in an electrochemical cell using UV light. The efficiencies of these processes are less than 1% even with UV light[57]. Thus, the approach in this work provides a promising alternative towards utilization of CO_2 to reduced forms using solar energy. Figure 9 (b) shows the dependence of light to chemical efficiency on H_2:CO_2 molar ratio at 200 °C. Because of the higher reaction order with respect to CO_2, a lower H_2:CO_2 results in higher light efficiency. At low H_2:CO_2 ratio of 0.25, we observed the highest light to chemical efficiency of 4.7%. At the same conditions, we obtained 13 times enhancement of reaction rate due to LSPR as shown in Figure S2.

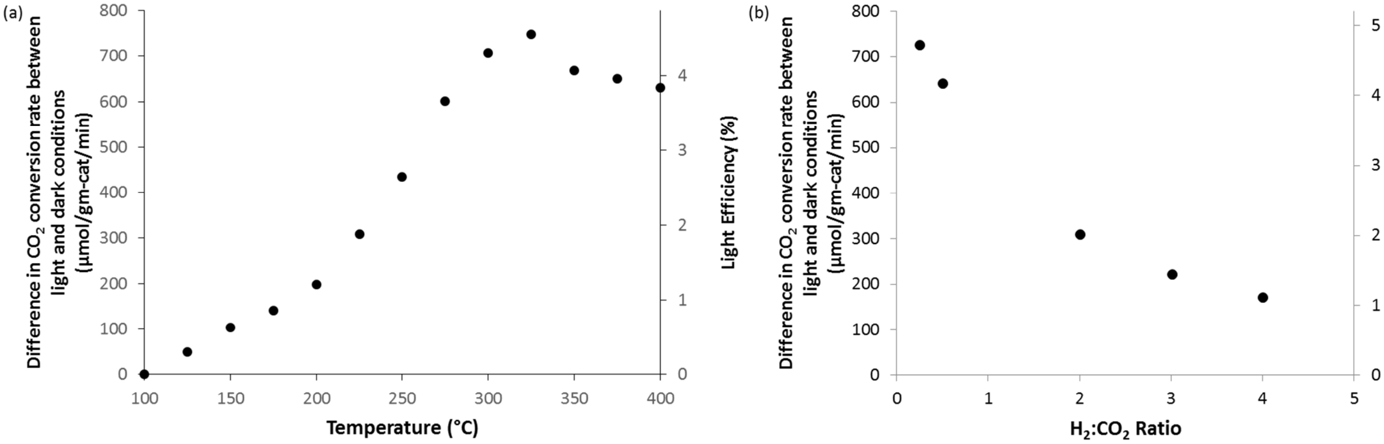

Figure 9. (a) Difference in CO_2 conversion rate between light and dark (Conversion rate due to light) vs. temperature in plasmon-enhanced reverse water gas shift reaction over Au/TiO_2 catalyst (primary axis) and Light to chemical efficiency corresponding to the conversion rate due to light (secondary axis). Experimental conditions: P= 110 psi, PP_{CO_2}=36.7 psi, PP_{H_2}= 73.3 psi, Total flow rate= 15 cm^3(STP)/min, catalyst amount= 7.4 mg. **(b)** Dependence of difference in reaction rates between light and dark reactions (primary axis) and light efficiency (secondary axis) on H_2:CO_2 ratio in plasmon enhanced reverse water gas shift reaction over Au/TiO_2 catalyst. Experimental conditions: P= 103 psi, T=200 °C, Total gas flow rate= 15 cm^3(STP)/min, catalyst amount= 7.9 mg.

4. Discussion

Three main effects have been reported in the literature to occur to explain how LSPR influences the reaction chemistry as shown in Figure 10. These effect are: (1) Intense scattering of the light (electromagnetic radiation) around the metal nanoparticle[58, 59], (2) electron-hole pair generation through electron excitation from the metal nanoparticle[21, 30, 60-62], and (3) localized heating effect resulting from dissipation of energy in phonons[31, 51, 52].

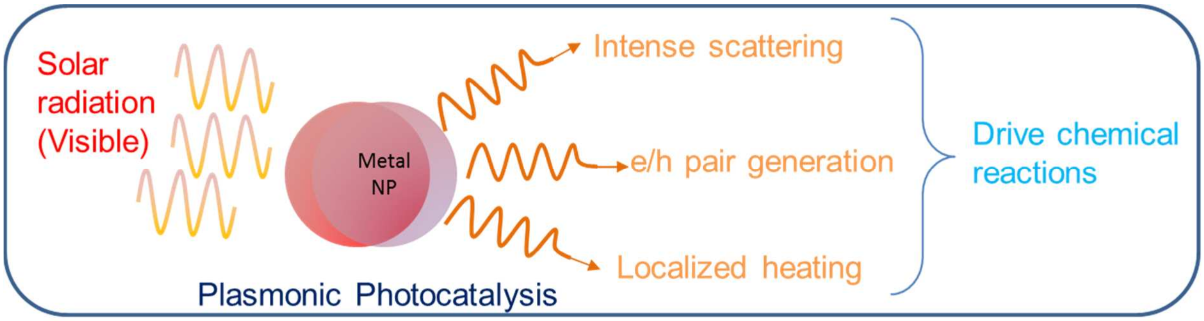

Figure 10. Effects of LSPR resulting in enhanced activity of plasmonic photocatalysts

Our reaction kinetics results show that the apparent activation energy and apparent reaction order with respect to CO_2 changes when visible light is used for Au/TiO_2 catalyzed RWGS reaction. These results suggest that the surface plasmons change the energetics of this reaction which could occur by two different processes: 1) the surface plasmons could modify the transition state of the rate determining steps or 2) the surface plasmons can modify the heat of adsorption of different reactants or intermediates. The reaction mechanism of WGS and RWGS has been extensively studied under dark conditions[38, 41-43, 63-67]. It is known that the WGS activity of Au catalysts is enhanced when it is supported on an oxide support like TiO_2 and CeO_2[41-44]. It has been proposed that the oxide support increases the activity of the Au catalysts by catalyzing the water dissociation step[42, 43, 68]. These studies propose that the WGS reaction over Au/TiO_2 goes through carboxyl and hydroxyl intermediates[42, 43, 68]. Burch showed that the dominant reactive intermediates depend upon the $H_2O:CO_2$ ratio in the reacting mixture[38, 69]. Under high $H_2O:CO_2$ ratio, hydroxyl species dominate the surface coverage; whereas under low $H_2O:CO_2$ ratios, carbonate/carboxyl species dominate the surface coverage[38]. It has also been proposed that the WGS reaction takes place at the interface of the gold and oxide support[42, 68]. Ribeiro and co-workers have shown that the activity of Au/TiO_2 catalysts for WGS reaction changes with Au particle size[70, 71]. They concluded that the corner and peripheral sites are the most active sites for the WGS reaction[70].

Consistent with these literature studies, Burch proposed a mechanism for dry RWGS reaction (low $H_2O:CO_2$ ratio) on Au/TiO_2 catalyst under dark conditions, as shown in Figure 11 and with Equations I-V[38]. The reaction proceeds by five elementary steps: (I) first, hydrogen dissociatively adsorbs on gold sites, (II) CO_2 adsorbs on oxygen vacancies on the metal oxide, (III) adsorbed H atoms react with adsorbed CO_2 molecule to form carboxyl species at sites on the interface of the metal oxide and gold, (IV) the carboxyl species dissociate to give gaseous CO and adsorbed OH on metal oxide sites, and (V) the adsorbed OH reacts with another adsorbed H atom to form H_2O at interfacial Au and metal oxide sites. These elementary steps are represented by Equations I-V, where * is a metal oxide (TiO_2) site, and x is a Au site. The equations for the surface coverage of adsorbed carbon dioxide and hydrogen are given by Equations 4 and 5, respectively. These equations assume that adsorption Steps I and II are in quasi-equilibrium. Equating the rates of Steps III, IV, and V, a rate expression for RWGS reaction can be derived as given by Equation 6.

$$H_2 + x \leftrightarrow 2 \times xH \qquad \text{(I)}$$

$$CO_2 + * \leftrightarrow CO_2^* \qquad \text{(II)}$$

$$CO_2^* + xH \rightarrow COOH^* + x \qquad \text{(III)}$$

$$COOH^* \rightarrow CO + OH^* \qquad \text{(IV)}$$

$$OH^* + xH \rightarrow H_2O + x + * \qquad \text{(V)}$$

$$\theta_{CO_2} = K_2 P_{CO_2} \theta_v \qquad (4)$$

$$x_H = \frac{\sqrt{K_1 P_{H_2}}}{1+\sqrt{K_1 P_{H_2}}} \qquad (5)$$

$$R_{RWGS} = \frac{K_2 k_3 P_{CO_2} x_H}{1+K_2 P_{CO_2}(1+k_3(\frac{1}{k_5}+\frac{x_H}{k_4}))} \qquad (6)$$

Table 2. Reaction rate equations for RWGS on Au/TiO$_2$ for various MASI assumptions

Case	MASI	Rate equation under dark		Proposed result of LSPR	Rate equation under light
1	OH^*	$R_{RWGS} = \frac{K_2 k_3 P_{CO_2} x_H}{1+\frac{K_2 k_3 P_{CO_2}}{k_5}}$	(7)	$k_5 \uparrow$	$K_2 k_3 P_{CO_2} x_H$
2	$COOH^*$	$R_{RWGS} = \frac{K_2 k_3 P_{CO_2} x_H}{1+\frac{K_2 k_3 P_{CO_2} x_H}{k_4}}$	(8)	$k_4 \uparrow$	$K_2 k_3 P_{CO_2} x_H$

Equation 6 can be further simplified by making assumptions about the most abundant surface intermediate (MASI). Table 2 shows the resulting rate equations assuming that either the OH* or COOH* is the MASI. The rate of RWGS reaction is given by the Equation 7 which assumes that OH* is the MASI. This expression can result in fractional order with respect to CO$_2$ if the ratio $K_2k_3P_{CO2}/k_5 \geq 1$. The apparent rate order with respect to CO$_2$ can change to 1.0, under light, if the LSPR increases the rate constants for Step V (i.e. k_5) more than any other steps. In case 2, COOH* is considered to be the MASI. With this assumption, the rate of RWGS reaction is given by Equation 8. If $K_2k_3P_{CO2}x_H/k_4 \geq 1$, then a fractional order with respect to CO$_2$ can be obtained. In this case, the apparent rate order with respect to CO$_2$ can change to 1.0, under light, if the LSPR increase the rate constant for Step IV (i.e. k_4) more than any other steps. The effect of light can be further evaluated by fitting the experimental data to a simple two constant linear rate equation shown in Equation 9. Table 3 illustrate how the rate and equilibrium constants in Equations 7 and 8 correspond to the slope and intercept in Equation 9.

$$\frac{1}{R_{RWGS}} = \frac{slope}{P_{CO_2}} + \text{intercept} \qquad (9)$$

Table 3. Interpretation of slope and intercept given in Equation 9 to kinetic parameters under different MASI assumptions

	OH MASI	**COOH MASI**
slope	$\frac{1}{K_2 k_3 x_H}$	$\frac{1}{K_2 k_3 x_H}$
intercept	$\frac{1}{k_5 x_H}$	$\frac{1}{k_4}$

The reaction kinetics data from Figure 8a at 200 °C were then fit to Equation 9. The fitting results are shown in parity plot given in Figure S3. The slope of the fit changes from 0.236±0.015 under dark to 0.111±0.002 under light. This change in slope corresponds to 2.1 times enhancement in the product of K$_2$,

k_3 and x_H. At the same time the intercept for the fit changed from 0.015±0.001 under dark to 0.00006±0.0002 under light. The change in the intercept corresponded to 242.9 times enhancement of either k_4 or k_5x_H. Thus, the LSPR affects the rates of Steps IV or V more than any other step involved in the catalytic mechanism. This increase in rate constants with LSPR corresponds to a decrease in activation energy of either Step IV or V of 21.6 kJ/mol.

In Figure 11 we illustrate the two possible mechanisms through which LSPR can increase these elementary Steps, IV and V. Hot electron generated from LSPR of Au can get transferred to the adsorbed OH or COOH species which accelerates the desorption of H_2O and CO, respectively. The electron affinity values of OH (1.827 eV)[72] and COOH (1.510 eV)[73] are higher than other species involved in this reaction mechanism (e.g. electron affinity of CO_2 is -0.922 eV and electron affinity of H is 0.754 eV)[73, 74]. Higher electron affinities of OH and COOH intermediates suggest that these species are more likely to accept the hot electrons generated by the LSPR and form transient negative ion (TNI). The formation of these TNI states has been proposed as one of the possible mechanisms for plasmonic enhancement in the recent studies[20, 75]. Alternatively, intense electromagnetic fields around Au nanoparticle can polarize the O-H or C-O bonds present in the OH* and COOH* intermediates as shown in Figure 11. This effect can facilitate the bond breaking steps and result in higher desorption rates. Both of these mechanisms could lower surface coverage of adsorbed species and explain changes in apparent rate orders and activation energy due to LSPR.

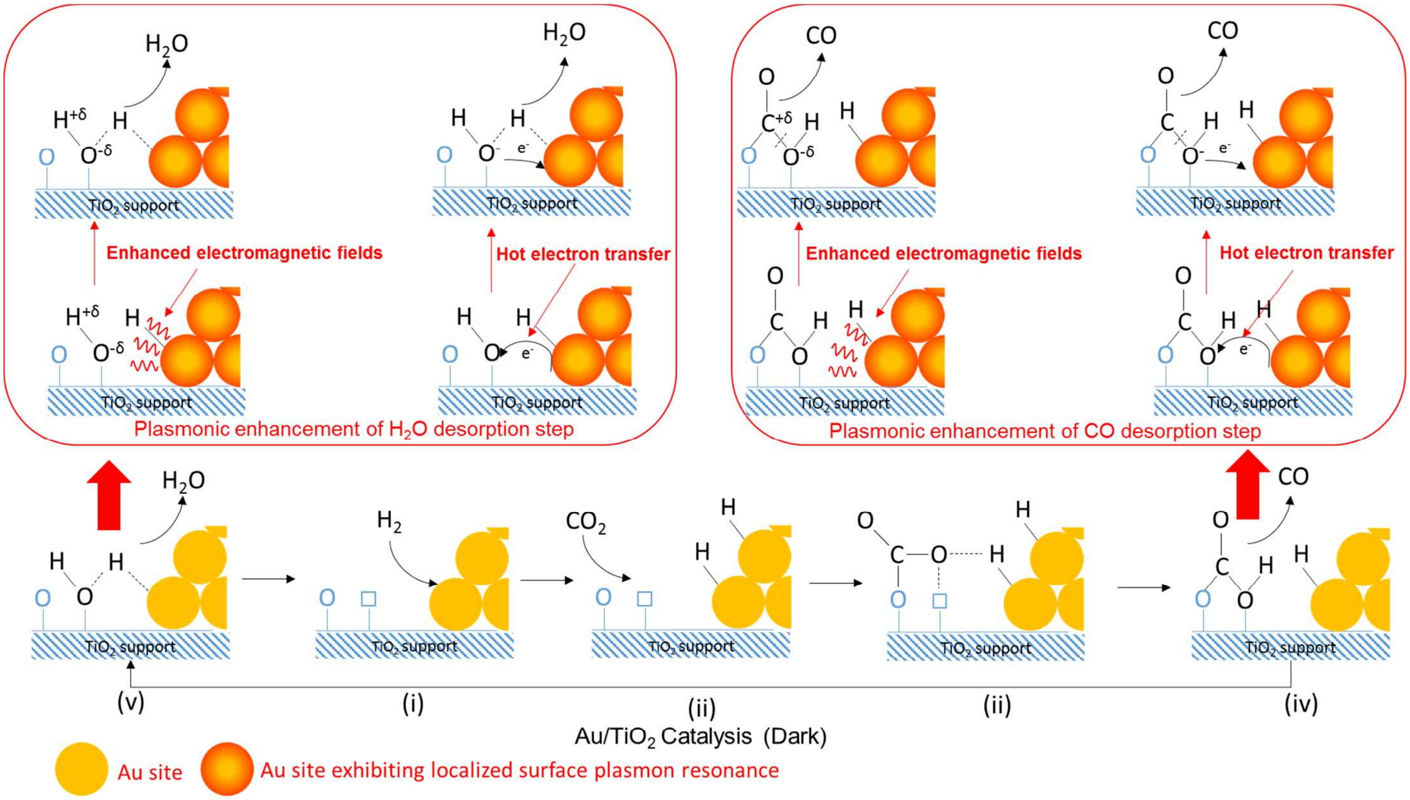

Figure 11. Proposed mechanism for plasmonic enhancement of reverse water gas shift reaction over Au/TiO_2 catalyst

5. Conclusion

We demonstrate that the localized surface plasmon resonance can increase the RWGS activity of Au supported catalysts by 30 to 1300% using visible light illumination. The enhancement was a function of the type of oxide support used. Au/TiO_2 and Au/CeO_2 showed the highest activity for RWGS reaction. A visible light to chemical efficiency of up to 5% for plasmonic RWGS reaction over Au/TiO_2 catalyst was observed. The LSPR causes a shift in the energetics of the reaction mechanism for the Au/TiO_2 catalyst. The apparent activation energy decreased from 47 kJ/mol to 35 kJ/mol with visible light for this catalyst. The reaction order with respect to CO_2 increased from 0.5 without visible light to 1.0 with visible light. The reaction order with respect to H_2 was similar with and without light. These results demonstrate that the LSPR changes the intrinsic reaction kinetics on the catalyst surface. Our analysis suggests that the LSPR increases the rate constants for either carboxyl decomposition or hydroxyl hydrogenation more than any other step in the RWGS mechanism. Both of these steps are proposed to occur at the interface of the Au and TiO_2. This rate enhancement could occur via either hot electron generation mechanism or adsorbate polarization mechanism resulting from LSPR.

6. Acknowledgements

This research was funded by the Advanced Research Projects Agency-Energy (ARPA-E), U.S. Department of Energy, under Award Number DE-AR0000329. We thank Hans-Joachim Freund and Manos Mavrikakis for helpful discussions about this topic.

Abbreviations

BID: Barrier-discharge ionization detector
DFT: Density functional theory
DP: Deposition precipitation
FTIR: Fourier transform infrared spectroscopy
GC: Gas chromatograph
I: Impregnation
ICP: Inductively coupled plasma
LSPR: Localized surface plasmon resonance
MASI: Most abundant surface intermediate
PID: Proportional integral derivative
RWGS: Reverse water gas shift
TEM: Transmission electron microscopy
TNI: Transient negative ion
UHP: Ultra high purity
UV: Ultraviolet
WGS: Water gas shift

Nomenclature

ΔH: Heat of reaction
Bi_w: Biot number at the wall
C_s: Concentration of reactant at the external surface of the catalyst particle
D_e: Effective diffusivity
E: Activation energy of the reaction
h: Heat transfer coefficient

K_c: Mass-transfer coefficient between the catalyst and bulk phases
k_i: forward rate constant for elementary step i
K_i: Equilibrium rate constant for elementary step i
k_e: Effective thermal conductivity of the catalyst bed
n: Reaction order
P_i: Partial pressure of reactant i
r''': Reaction rate per catalyst volume
R: Universal gas constant
R_o: Outer radius of reactor
r_p: Catalyst particle radius
T_b: Temperature of bulk phase
T_s: Catalyst surface temperature
T_w: Reactor wall temperature
x_H: Surface coverage of H on Au
θ_i: Surface coverage of species i on the catalyst support

References

1. N. S. Lewis and G. Crabtree, *Basic Research Needs for Solar Energy Utilization*, 2005.
2. N. S. Lewis and D. G. Nocera, *Proceedings of the National Academy of Sciences*, 2006, **103**, 15729-15735.
3. NREL, Best Research-Cell Efficiencies, http://www.nrel.gov/ncpv/images/efficiency_chart.jpg, Accessed 03/03/2014, 2014.
4. M. G. Walter, E. L. Warren, J. R. McKone, S. W. Boettcher, Q. Mi, E. A. Santori and N. S. Lewis, *Chem. Rev.*, 2010, **110**, 6446-6473.
5. K. Maeda, K. Teramura, D. L. Lu, T. Takata, N. Saito, Y. Inoue and K. Domen, *Nature*, 2006, **440**, 295-295.
6. A. Kudo and Y. Miseki, *Chem. Soc. Rev.*, 2009, **38**, 253-278.
7. A. Fujishima and K. Honda, *Nature*, 1972, **238**, 37-38.
8. M. Gratzel, *Nature*, 2001, **414**, 338-344.
9. G. Centi, E. A. Quadrelli and S. Perathoner, *Energy Environ. Sci.*, 2013, **6**, 1711-1731.
10. G. Centi, G. Iaquaniello and S. Perathoner, *ChemSusChem*, 2011, **4**, 1265-1273.
11. G. Centi and S. Perathoner, *Catal. Today*, 2009, **148**, 191-205.
12. A. Corma and H. Garcia, *J. Catal.*, 2013, **308**, 168-175.
13. C. Bartholomew and R. J. Farrauto, *Fundamentals of Industrial Catalytic Processes*, Wiley, New Jersey, 2006.
14. U. N. D. Program, *World Energy Assessment Report: Energy and the Challenge of Sustainability*, United Nations, New York, 2003.
15. X. H. Wang, J. G. Li, H. Kamiyama, Y. Moriyoshi and T. Ishigaki, *Journal of Physical Chemistry B*, 2006, **110**, 6804-6809.
16. F. E. Osterloh, *Chem. Soc. Rev.*, 2013, **42**, 2294-2320.
17. A. K. L. Sajjad, S. Shamaila, B. Z. Tian, F. Chen and J. L. Zhang, *Journal of Hazardous Materials*, 2010, **177**, 781-791.
18. M. Grätzel, *Inorganic Chemistry*, 2005, **44**, 6841-6851.
19. S. Linic, P. Christopher and D. B. Ingram, *Nature Materials*, 2011, **10**, 911-921.
20. P. Christopher, H. Xin and S. Linic, *Nat Chem*, 2011, **3**, 467-472.
21. F. Sastre, M. Oteri, A. Corma and H. Garcia, *Energy Environ. Sci.*, 2013, **6**, 2211-2215.

22. S. Mukherjee, F. Libisch, N. Large, O. Neumann, L. V. Brown, J. Cheng, J. B. Lassiter, E. A. Carter, P. Nordlander and N. J. Halas, *Nano Letters*, 2012, **13**, 240-247.
23. W. B. Hou and S. B. Cronin, *Advanced Functional Materials*, 2013, **23**, 1612-1619.
24. Z. Liu, W. Hou, P. Pavaskar, M. Aykol and S. B. Cronin, *Nano Letters*, 2011, **11**, 1111-1116.
25. W. H. Hung, M. Aykol, D. Valley, W. Hou and S. B. Cronin, *Nano Letters*, 2010, **10**, 1314-1318.
26. M. I. Stockman, *Opt. Express*, 2011, **19**, 22029-22106.
27. P. Christopher, H. Xin, A. Marimuthu and S. Linic, *Nat Mater*, 2012, **11**, 1044-1050.
28. K. A. Willets and R. P. Van Duyne, in *Annual Review of Physical Chemistry*, Annual Reviews, Palo Alto, 2007, vol. 58, pp. 267-297.
29. L. Wang, C. Clavero, Z. Huba, K. J. Carroll, E. E. Carpenter, D. Gu and R. A. Lukaszew, *Nano Letters*, 2011, **11**, 1237-1240.
30. X. M. Zhang, Y. L. Chen, R. S. Liu and D. P. Tsai, *Reports on Progress in Physics*, 2013, **76**.
31. C. Wang, O. Ranasingha, S. Natesakhawat, P. R. Ohodnicki, Jr., M. Andio, J. P. Lewis and C. Matranga, *Nanoscale*, 2013, **5**, 6968-6974.
32. R. Zanella, S. Giorgio, C. H. Shin, C. R. Henry and C. Louis, *J. Catal.*, 2004, **222**, 357-367.
33. R. Zanella, S. Giorgio, C. R. Henry and C. Louis, *Journal of Physical Chemistry B*, 2002, **106**, 7634-7642.
34. D. L. Nguyen, S. Umbarkar, M. K. Dongare, C. Lancelot, J. S. Girardon, C. Dujardin and P. Granger, *Catalysis Communications*, 2012, **26**, 225-230.
35. F. Boccuzzi, A. Chiorino, G. Martra, M. Gargano, N. Ravasio and B. Carrozzini, *J. Catal.*, 1997, **165**, 129-139.
36. X. Zhou, G. Liu, J. Yu and W. Fan, *Journal of Materials Chemistry*, 2012, **22**, 21337-21354.
37. A. Marimuthu, J. Zhang and S. Linic, *Science*, 2013, **339**, 1590-1593.
38. R. Burch, *Phys. Chem. Chem. Phys.*, 2006, **8**, 5483-5500.
39. M. Haruta and M. Daté, *Applied Catalysis A: General*, 2001, **222**, 427-437.
40. M. S. Chen and D. W. Goodman, *Catalysis Today*, 2006, **111**, 22-33.
41. J. A. Rodriguez, S. D. Senanayake, D. Stacchiola, P. Liu and J. Hrbek, *Accounts of Chemical Research*, 2013.
42. J. A. Rodriguez, J. Evans, J. Graciani, J.-B. Park, P. Liu, J. Hrbek and J. Fdez Sanz, *Journal of Physical Chemistry C*, 2009, **113**, 7364-7370.
43. J. A. Rodriguez, S. Ma, P. Liu, J. Hrbek, J. Evans and M. Perez, *Science*, 2007, **318**, 1757-1760.
44. Q. Fu, H. Saltsburg and M. Flytzani-Stephanopoulos, *Science*, 2003, **301**, 935-938.
45. D. E. Mears, *Industrial & Engineering Chemistry Process Design and Development*, 1971, **10**, 541-547.
46. M. E. Davis and R. J. Davis, *Fundamentals of Chemical Reaction Engineering*, McGraw-Hill Higher Education, 2002.
47. M. Vannice, *Kinetics of Catalytic Reactions*, Springer New York, 2005.
48. , Aspen Plus v7.3, Aspen Technology, Inc., Cambridge, MA, 2011.
49. A. Cybulski, M. J. Van Dalen, J. W. Verkerk and P. J. Van Den Berg, *Chemical Engineering Science*, 1975, **30**, 1015-1018.
50. P. B. Weisz and C. D. Prater, in *Advances in Catalysis*, eds. V. I. K. W.G. Frankenburg and E. K. Rideal, Academic Press, 1954, vol. Volume 6, pp. 143-196.
51. C. W. Yen and M. A. El-Sayed, *Journal of Physical Chemistry C*, 2009, **113**, 19585-19590.
52. J. R. Adleman, D. A. Boyd, D. G. Goodwin and D. Psaltis, *Nano Lett.*, 2009, **9**, 4417-4423.
53. C. Tabor, W. Qian and M. A. El-Sayed, *Journal of Physical Chemistry C*, 2007, **111**, 8934-8941.
54. A. O. Govorov and H. H. Richardson, *Nano Today*, 2007, **2**, 30-38.
55. O. Hougen and K. Watson, *Chemical Process Principles. Part 3. Kinetics and Catalysis*, Wiley, New York, 1947.

56. M. Manzoli, A. Chiorino, F. Vindigni and F. Boccuzzi, *Catalysis Today*, 2012, **181**, 62-67.
57. S. C. Roy, O. K. Varghese, M. Paulose and C. A. Grimes, *ACS Nano*, 2010, **4**, 1259-1278.
58. F. Le, D. W. Brandl, Y. A. Urzhumov, H. Wang, J. Kundu, N. J. Halas, J. Aizpurua and P. Nordlander, *Acs Nano*, 2008, **2**, 707-718.
59. S. L. Zou and G. C. Schatz, *Chemical Physics Letters*, 2005, **403**, 62-67.
60. J. Sa, G. Tagliabue, P. Friedli, J. Szlachetko, M. H. Rittmann-Frank, F. G. Santomauro, C. J. Milne and H. Sigg, *Energy & Environmental Science*, 2013, **6**, 3584-3588.
61. K. H. Kim, K. Watanabe, D. Menzel and H.-J. Freund, *Surf. Sci.*, 2012, **606**, 1142-1151.
62. K. Watanabe, D. Menzel, N. Nilius and H.-J. Freund, *Chem. Rev.*, 2006, **106**, 4301-4320.
63. N. Schumacher, A. Boisen, S. Dahl, A. A. Gokhale, S. Kandoi, L. C. Grabow, J. A. Dumesic, M. Mavrikakis and I. Chorkendorff, *J. Catal.*, 2005, **229**, 265-275.
64. A. A. Gokhale, J. A. Dumesic and M. Mavrikakis, *Journal of the American Chemical Society*, 2008, **130**, 1402-1414.
65. R. J. Madon, D. Braden, S. Kandoi, P. Nagel, M. Mavrikakis and J. A. Dumesic, *J. Catal.*, 2011, **281**, 1-11.
66. L. C. Grabow, A. A. Gokhale, S. T. Evans, J. A. Dumesic and M. Mavrikakis, *The Journal of Physical Chemistry C*, 2008, **112**, 4608-4617.
67. T. Tabakova, F. B. Boccuzzi, M. Manzoli and D. Andreeva, *Appl. Catal. A-Gen.*, 2003, **252**, 385-397.
68. A. Hussain, J. Gracia, B. E. Nieuwenhuys and J. W. Niemantsverdriet, *ChemCatChem*, 2013, **5**, 2479-2488.
69. F. C. Meunier, D. Tibiletti, A. Goguet, D. Reid and R. Burch, *Appl. Catal. A-Gen.*, 2005, **289**, 104-112.
70. M. Shekhar, J. Wang, W. S. Lee, W. D. Williams, S. M. Kim, E. A. Stach, J. T. Miller, W. N. Delgass and F. H. Ribeiro, *Journal of the American Chemical Society*, 2012, **134**, 4700-4708.
71. W. D. Williams, M. Shekhar, W.-S. Lee, V. Kispersky, W. N. Delgass, F. H. Ribeiro, S. M. Kim, E. A. Stach, J. T. Miller and L. F. Allard, *Journal of the American Chemical Society*, 2010, **132**, 14018-14020.
72. J. R. Smith, J. B. Kim and W. C. Lineberger, *Physical Review A*, 1997, **55**, 2036-2043.
73. NIST, *NIST Chemistry Webbook*, 2014.
74. C.-G. Zhan, J. A. Nichols and D. A. Dixon, *The Journal of Physical Chemistry A*, 2003, **107**, 4184-4195.
75. S. Linic, P. Christopher and D. B. Ingram, *Nat Mater*, 2011, **10**, 911-921.
76. D. E. Mears, *J. Catal.*, 1971, **20**, 127-131.
77. J. B. Anderson, *Aiche J.*, 1962, **18**, 147-148.